

What contributes to the interannual variability in tropical lower stratospheric temperatures?

Alison Ming¹ and Peter Hitchcock²

¹University of Cambridge

²Cornell University

November 24, 2022

Abstract

The interannual variability in mid and lower stratospheric temperatures for the period 1984–2019 is decomposed into dynamical and radiative contributions using a radiative calculation perturbed with changes in dynamical heating, trace gases and aerosol optical depth. The temperature timeseries obtained is highly correlated with the de-seasonalised ERA5 temperature ($r^2 > 0.6$ for 1995 to 2019 in the region 15 to 70 hPa). Contributions from ozone and dynamical heating are found to be of similar importance, with water vapor, stratospheric aerosols, and carbon dioxide playing smaller roles. Prominent aspects of the temperature timeseries are closely reproduced, including the 1991 Pinatubo volcanic eruption, the year-2000 water vapour drop, and the 2016 Quasi-biennial oscillation (QBO) disruption. Ozone below 20 hPa is primarily controlled by transport and is positively correlated to the upwelling. This ozone-transport feedback acts to increase the temperature response to a change in upwelling by providing an additional ozone-induced radiative temperature change. This can be quantified as an enhancement of the dynamical heating of about 20% at 70 hPa. A principle oscillation pattern (POP) analysis is used to estimate the contribution of the ozone QBO (± 1 K at 70 hPa). The non-QBO ozone variability is also shown to be significant. Using the QBO leading POP timeseries as representative of the regular QBO signal, the QBO 2016 disruption is shown to have an anomalously large radiative impact on the temperature due to the ozone change (> 3 K at 70 hPa).

What contributes to the interannual variability in tropical lower stratospheric temperatures?

Alison Ming¹, Peter Hitchcock²

¹Department of Applied Mathematics and Theoretical Physics, University of Cambridge, Cambridge, UK

²Cornell University, Ithaca, New York, USA

Key Points:

- Interannual variability in lower tropical stratospheric temperatures has been reconstructed.
- Ozone and dynamical heating dominate. Aerosol and water vapor contributions are not negligible.
- Ozone associated with the QBO contributes substantially, particularly during the 2016 disruption.

Corresponding author: Alison Ming, A.Ming@damtp.cam.ac.uk

Abstract

The interannual variability in mid and lower stratospheric temperatures for the period 1984–2019 is decomposed into dynamical and radiative contributions using a radiative calculation perturbed with changes in dynamical heating, trace gases and aerosol optical depth. The temperature timeseries obtained is highly correlated with the de-seasonalised ERA5 temperature ($r^2 > 0.6$ for 1995 to 2019 in the region 15 to 70 hPa). Contributions from ozone and dynamical heating are found to be of similar importance, with water vapor, stratospheric aerosols, and carbon dioxide playing smaller roles. Prominent aspects of the temperature timeseries are closely reproduced, including the 1991 Pinatubo volcanic eruption, the year-2000 water vapour drop, and the 2016 Quasi-biennial oscillation (QBO) disruption.

Ozone below 20 hPa is primarily controlled by transport and is positively correlated to the upwelling. This ozone-transport feedback acts to increase the temperature response to a change in upwelling by providing an additional ozone-induced radiative temperature change. This can be quantified as an enhancement of the dynamical heating of about 20% at 70 hPa.

A principal oscillation pattern (POP) analysis is used to estimate the contribution of the ozone QBO (± 1 K at 70 hPa). The non-QBO ozone variability is also shown to be significant. Using the QBO leading POP timeseries as representative of the regular QBO signal, the QBO 2016 disruption is shown to have an anomalously large radiative impact on the temperature due to the ozone change (> 3 K at 70 hPa).

Plain Language Summary

Temperatures in the lower stratosphere vary substantially from year to year and play a major role in determining the composition of the stratosphere, which in turn plays an important role in Earth’s energy budget. Understanding this variability is thus key to understanding the properties of the stratosphere. We calculate the amount of heating due to changes in four main factors (circulation, ozone, water vapour and aerosol). This allows us to decompose the observed temperature changes into these main factors with good agreement during the time period studied (1984–2019). Our method also allows us to analyse anomalously large temperature changes such as those during volcanic eruptions and the recent disruption in the Quasi-biennial oscillation. We find that ozone changes play a key role throughout the time period analysed. Our findings indicate that temperature changes related to composition (particularly ozone) are critical in determining the variability of temperatures in the lower tropical stratosphere. They highlight the need to validate these processes in global models.

1 Introduction

The interannual variability of temperatures in the tropical lower stratosphere is of interest since the temperature in this region controls the entry of water vapour into the stratosphere which can then modify the surface radiative balance (Fueglistaler et al., 2014). The chemical composition of the stratosphere is strongly impacted by the balance reached between the circulation, radiation, temperatures, and chemistry in this region. A number of trace species including ozone, water vapour, and stratospheric aerosols in this region have significant climate impacts. The temperatures in the tropical lower stratosphere are closely coupled to these trace gases and thus to their influence on the energy balance of the climate system. Furthermore, temperatures in this region exhibit more uncertainty in reanalyses than in any other region in the atmosphere below 10 hPa (see Hersbach et al., 2020, their Fig. 11). A detailed understanding of the processes that determine temperatures in this region is thus desirable.

The interannual variability in dynamical heating arising from changes in upwelling in the Brewer-Dobson circulation has been identified as a main contributor to the temperature variability (Fueglistaler et al., 2014). An increase in upwelling decreases the temperature. It also changes the transport of ozone, water vapour and aerosol—all radiatively active trace species. These gases induce local and non-local changes to the radiative balance. Several studies have focused on this interaction in the tropical lower stratosphere in the time mean and for the annual cycle (Forster et al., 2007; Ming et al., 2017; Charlesworth et al., 2019). These studies make use of single column radiative calculations, typically assuming that the dynamical heating is fixed, and have proved to be instrumental in understanding the contribution of radiative transfer to temperature variability in this region.

This work builds on previous such studies but focuses on quantifying the different contributions of the dynamical heating and the radiative heating to the temperature interannual variability. As observation systems and reanalysis models have improved, the temperature variability in the tropical lower stratosphere has become better constrained with good agreement between the modern reanalysis datasets (ERA-Interim, ERA5, JRA-55, MERRA-2, and CFSR) and radio occultation measurements particularly after the year 2000 (Tegtmeier et al., 2020). Since temperature is well constrained and dynamically linked to the upwelling and radiatively linked to changes in trace gases, understanding the temperature variability is particularly relevant to elucidating the properties of the Tropical Tropopause Layer (TTL) (Fueglistaler et al., 2014).

In this study, we test the importance of large scale upwelling and trace gas changes to the temperature variability using a single column clear-sky radiative code that is continuously perturbed. We show that we can successfully reconstruct the time series of interannual variability and quantify the contributions of the various perturbations. We demonstrate that ozone changes are of similar importance to dynamical variability on interannual timescales, extending results from previous studies that emphasised the role of ozone in determining the time-mean structure of the TTL (Thuburn & Craig, 2002; Charlesworth et al., 2019) and the large seasonal cycle in TTL temperatures (Ming et al., 2017; Gilford & Solomon, 2017).

A significant part of the ozone variability is driven by the Quasi-biennial oscillation (QBO). The QBO is characterized by descending bands of zonal winds, alternating between eastward and westward. Eastward (vertical) shear is associated with anomalously warm temperatures, while westward shear is associated with anomalously cold temperatures, consistent with thermal wind balance. These are further associated with a secondary meridional circulation (Plumb & Bell, 1982), with relative ascent in eastward shear zones and descent in westward shear zones. Since transport dominates the budget of ozone below about 20 hPa, this secondary circulation contributes to ozone variability, with increased ascent bringing up relatively ozone poor air. Hence there is a large component of QBO variability in ozone (Pahlavan et al., 2021). We find that although a large part of the ozone variability is indeed related to the QBO, a large non-QBO component is also present. Both contribute substantially to interannual variability in temperatures.

Another important contribution arises from explosive volcanic eruptions that emit aerosol into the stratosphere. This aerosol warms the lower stratosphere. During the time period we analyse, the Pinatubo eruption in 1991 is the largest contributor, although the effects of smaller eruptions are also notable. By including a simple representation of the eruptions using the observed aerosol optical depth, we are able to reproduce the observed temperature signal following the volcanic eruption.

The other contributions to the temperature come from water vapour variations which are modulated by the temperatures at the cold point and from the increase in carbon dioxide in the atmosphere.

The calculations in this work make a clear sky assumption and do not explicitly simulate dynamics or transport. Instead we impose distributions of trace species from observations and adiabatic heating inferred from ascent taken from the ERA5 reanalysis. The calculations do not explicitly model potential feedbacks between these drivers, such as transport effects or meridional circulations driven by diabatic heating. Nonetheless our calculation does provide insight into these interactions. We find that the ozone change amplifies the temperature response to the dynamical heating. Increases in upwelling are correlated to decreases in ozone. Both of these changes lead to a decrease in temperature. This positive feedback of ozone onto the temperatures can be described as an increase in radiative timescales or as an increase in the effective dynamical heating and we present estimates of these quantities.

The paper is organised as follows. Section 2 describes the methodology that extends single column radiative calculations to interannually varying perturbations. Section 3 describes the data and radiative code. We discuss the contributions of various perturbations to the temperature in Section 4 and quantify the QBO contribution in Section 5. The QBO 2016 disruption is studied in more detail in Section 5.1. Section 6 focuses on the modification of radiative damping resulting from ozone. Finally, in Section 7, we discuss and summarise our results. We also provide a supplementary information file that contains additional plots of relevance.

2 interannually evolving fixed dynamical heating

A common method for estimating the temperature change resulting from a perturbation in trace gas is the Fixed Dynamical Heating (FDH) calculation. The FDH calculation assumes that for a given perturbation, the dynamical heating remains the same as the unperturbed state, allowing the new temperature required to reach radiative equilibrium to be calculated. This method was modified by Forster and Shine (1997) to study seasonally evolving forcings by allowing the dynamical heating to evolve with time and iterating to a new seasonal cycle in temperatures and is called the seasonally evolving fixed dynamical heating (SEFDH) calculation. The SEFDH calculation has provided insight into radiative processes at play in the tropical lower stratosphere on seasonal timescales. We further modify this calculation and introduce the interannually evolving fixed dynamical heating calculation (IEFDH), described below, as method of estimating the contributions of interannually varying changes in trace gas concentrations on temperatures.

The thermodynamic equation in the Transformed Eulerian Mean framework (Andrews et al., 1987), neglecting eddy terms, is

$$\partial_t \bar{T} = \bar{Q}_{\text{rad}} - \bar{w}^* \bar{S} - \bar{v}^* \partial_y \bar{T} = \bar{Q}_{\text{rad}} + \bar{Q}_{\text{dyn}}, \quad (1)$$

which predicts the rate of change of zonal mean temperature, \bar{T} , with time, t where $\bar{(\cdot)}$ represents a zonal mean. The dynamical heating, \bar{Q}_{dyn} , is defined by the second equality in Eq. (1). \bar{v}^* and \bar{w}^* are the horizontal and vertical components of the mean residual velocity respectively. y is the meridional coordinate. $\bar{S} = \partial_z \bar{T} + \kappa \bar{T} / H$ is a measure of the static stability where z is the log-pressure height. $z = -H \log(\sigma)$ where H is a scale height taken to be 7 km and $\sigma = p/p_0$ where p is pressure and $p_0 = 1000$ hPa. $\kappa = R/c_p \simeq 2/7$ where R is the gas constant for dry air and c_p is the specific heat at constant pressure. The radiative heating, \bar{Q}_{rad} , depends, in general, on the temperature and the distributions of various radiatively active components including clouds, aerosols and trace gases. The meridional advection term in (1) is small and is neglected in this work.

In the unperturbed, equilibrium state of the stratosphere, the radiative and dynamical heating rates balance, Equation 2:

$$\bar{Q}_{\text{dyn}}^0 + \bar{Q}_{\text{rad}}(\bar{\chi}^0, \bar{T}^0) = 0 \quad (2)$$

where χ represents the trace gas mixing ratios and $(\cdot)^\circ$ denotes the time mean state. The dynamical heating is calculated from this equation and assumed to be fixed.

The system is then perturbed by imposing the interannual variation in a trace gas, χ , in the stratosphere. The new radiative heating is calculated and Equation 3 is used to iterate the temperature forward:

$$\partial_t \bar{T} = \bar{Q}_{\text{dyn}}^0 + Q_{\text{rad}}(\bar{\chi}, \bar{T}) \quad (3)$$

Note that unlike the FDH and SEFDH methods, the IEFDH calculation does not reach equilibrium as the system is continuously being perturbed. This means that for the first few months, the calculated temperatures is depend on the initial condition.

Finally, following a similar method to Ming et al. (2017) we also impose the interannual variation in the dynamical heating, \bar{Q}_{dyn} , as a perturbation to Equation (3) to estimate the temperature change associated with the upwelling.

3 Data and Methods

Ozone and water vapour mixing ratios are obtained from the Stratospheric Water and OzOne Satellite Homogenized (SWOOSH) dataset (Davis et al., 2016; Tummon et al., 2015) which is formed from a combination of measurements from five limb and solar occultation satellites from 1984 to 2015, namely: SAGE-II/III, UARS HALOE, UARS MLS, and Aura MLS instruments. Values below 316 hPa are obtained by linear interpolation to the surface values from the ERA5 dataset. The results in this paper are not sensitive to this choice of method for in-filling tropospheric data. Stratospheric aerosol optical depth at 525 nm is obtained from GloSSAC v2.0 (Kovilakam et al., 2020; NASA/LARC/SD/ASDC, 2018). The interannual variations in ozone and water vapour are plotted in Figures S1 and S2 respectively.

Temperature and dynamical data are taken from the ERA-5 reanalysis dataset covering the period 1984 to 2019 (with ERA 5.1 for the period 2000 to 2006) ((C3S), 2017), using data retrieved at a horizontal resolution of 1° , at 3-hourly analysis time intervals and on 137 model levels. Transformed Eulerian Mean quantities are calculated on the original retrieved data before being interpolated to the grids used in the radiative calculations described below. Since we are focusing on the interannual variability, the data is smoothed by computing monthly averages and then linearly interpolating to daily values. Trends in the various quantities are not removed except where explicitly stated.

The radiative calculations use the Morcrette (1991) radiation scheme, which includes updates to the longwave absorption properties of water vapour (Zhong and Haigh, 1995). All calculations use zonal mean data at 5° intervals in latitude, on 100 pressure levels and run from 1984 to 2016. In the shortwave, a three point Gaussian quadrature method is used to account for the diurnal variation in the solar zenith angle. The albedo time series is taken from ERA5 reanalysis data. Carbon dioxide is assumed to be well mixed. The volume mixing ratio is set to 345 ppmv for all calculations except for the experiment where CO_2 is changed. In this experiment, we assume that CO_2 has increased linearly from 345 ppmv (1984 value) to 412 ppmv (2019 value) and calculate the temperature change using a simple FDH calculation.

Similar to other fixed dynamical heating calculations (Forster et al., 2007; Ming et al., 2017), we choose 130 hPa as the level above which the temperatures will be adjusted and below which temperatures will remained fixed to the time mean. All the perturbations add linearly to give the total (not shown).

4 IEFDH results

The temperature interannual variability is reconstructed using the dynamical heating perturbation taken from ERA-5, ozone, water vapour, aerosol optical depth and carbon dioxide perturbations (labelled as the "all perturbations" experiment). Figure 1 shows the ERA-5 temperature interannual variability averaged between 30° N – S together with the corresponding temperature time series re-constructed using the IEFDH calculation with all the perturbations listed above.

The figure shows that these perturbations together capture the interannual variability in temperatures in the tropical lower and mid stratosphere with broadly good agreement throughout most of the time series after 1991 ($r^2 > 0.67$ in the region 20 to 70 hPa for 1992 to 2019, see Appendix Appendix A). The mean temperature from the IEFDH calculation before 1991 is about 0.9 K lower than ERA5. This could be due to a number of factors. For instance, reanalysis datasets are known to have jumps in the data when new instruments are assimilated and a clear jump is visible in the global mean anomalies of temperature and ozone in ERA5 before and after the Pinatubo volcanic eruption in 1991 (Hersbach et al., 2020, their figure 25). In the IEFDH calculation, the SWOOSH dataset chooses SAGE II ozone as the mean reference satellite against which ozone from UARS MLS and UARS HALOE is adjusted. These satellites became operational in October 1991. Identifying the cause of this jump is beyond the scope of the present study, but if we account for this jump by applying a constant offset, we find that the interannual variability in ERA5 is captured by the IEFDH calculation before 1991. The difference between the ERA5 temperature and the IEFDH calculation is shown in Figure S3 in the supplementary information.

Next we turn to a discussion of the dominant processes that contribute to this interannual variability.

4.1 Dynamical heating and ozone

Between 1984 and 2019, the temperature at 70 hPa varies by ± 2.9 K in ERA5 and by ± 2.7 K in the IEFDH all perturbation experiment as shown in Figure 2(a). Figures 2(b) and (c) break down the temperature time series into the contributions from the different perturbations. The equivalent plot for 90 hPa can be found in Figure S4. A contributor is the dynamical heating perturbation (± 2.1 K) which is consistent with the findings of Fueglistaler et al. (2014, their Fig. 3). However, variations in ozone generate a comparable contribution to the temperature variation throughout the time series, of up to ± 1.6 K. In the tropical lower stratosphere, an increase in ozone results in increased absorption of shortwave radiation and upwelling longwave radiation with the longwave heating dominating (about 80%). A detailed description of the radiative processes in this region can be found in the appendix of Ming et al. (2017).

During certain time periods, the temperature changes due to ozone are as large as that from the dynamical heating. Two examples of this are around the year 2000, roughly coinciding with a drop in water vapor (Randel et al., 2006), and during the 2015–16 disruption of the QBO (each of these features is discussed further below). Furthermore, ozone lags behind the dynamical heating by roughly 1 month. This is expected, since increased upwelling means less dynamical heating and more upward transport of ozone poor tropospheric air from below. We quantify this ozone-transport feedback further in Section 6.

This correlation does not always hold in the time series: anomalous dynamical warming in 2006 was not accompanied by ozone effects, nor were brief periods of dynamical cooling in 1996 and 1998. The correlation between the two effects was more substantially disrupted for nearly four years following the eruption of Mt. Pinatubo in 1991.

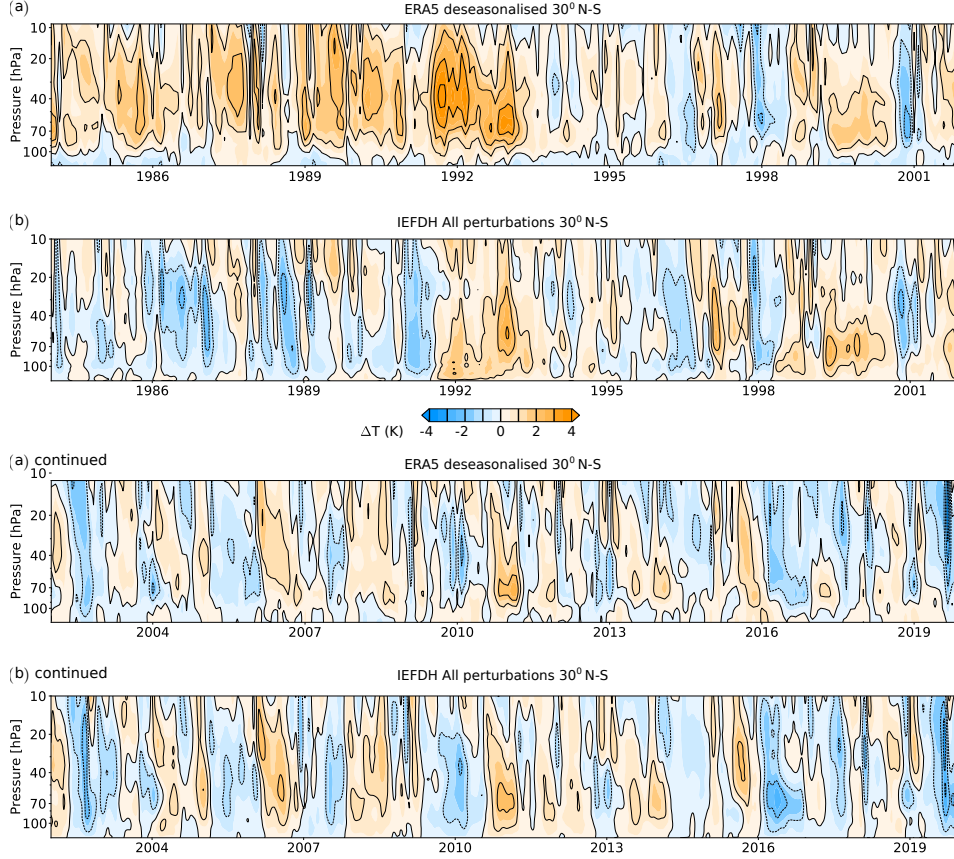


Figure 1. Interannual variability in temperature averaged between 30° N – S at different pressure levels from (a) ERA5 (b) the IEFDH radiative calculation with all perturbations. Differences are evaluated with respect to the reference period 2002–2010. Note that the plots are split into two panels spanning 1984 to 2001 and 2002 to 2019 for clarity. See main text for further details.

4.2 Water vapour

Water vapour variations in the tropical lower stratosphere are controlled by the temperature variations at the cold point where excess water vapour is freeze-dried out of the upwelling air. This pattern of water vapour variation is then advected upwards in what is known as the water vapour tape-recorder signal (Mote et al., 1994). An increase in water vapour leads to increased local longwave emission which dominates over the increased local absorption of upwelling radiation leading, in turn, to a drop in temperatures (Ming et al., 2017). The interannual variability in water vapour produces an IEFDH temperature change of about ± 0.4 K.

A series of drops in water vapour have been observed in the time series. The most prominent drop was in the year 2000 (Randel et al., 2006) and persisted until 2005. Lower temperatures at the cold point after the year 2000 gave rise to less water vapour entering the stratosphere which in turn led to a slight radiatively induced warming at 70 hPa. Various possible changes have been identified as the cause of the drop including increases in the Brewer-Dobson circulation (Dhomse et al., 2008), a strong El Niño followed by a La Niña and a change in the QBO phase (Garfinkel et al., 2018; Brinkop et al., 2016). The radiative impact on the surface of stratospheric water vapour changes are significant and have been quantified (Maycock et al., 2014; Gilford et al., 2016).

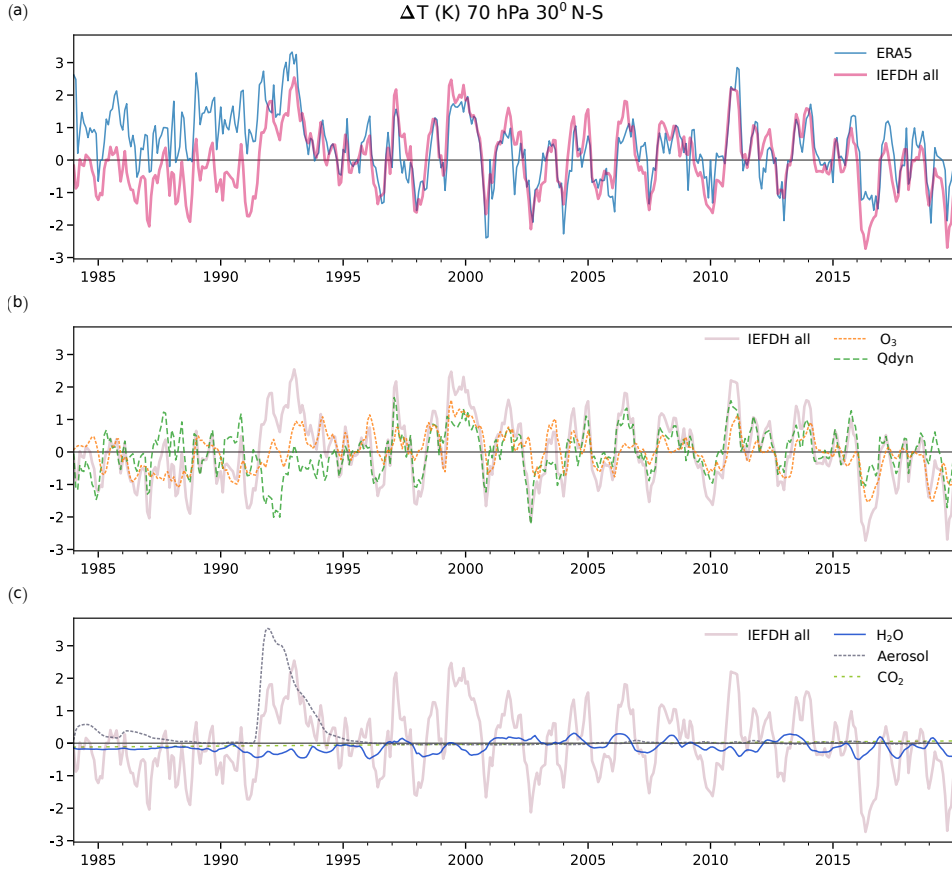


Figure 2. Interannual variability in temperature averaged between 30° N – S at 70 hPa, evaluated with respect to the reference period 2002–2010 for (a) ERA5 (cyan line) and the IEFDH all perturbations radiative calculation (thick pink line). The individual contributions to the total are broken down into the those from (b) ozone (orange dotted line) and dynamical heating (green dashed line) and (c) water vapour (blue solid line), aerosol (dotted grey line) and carbon dioxide (green dashed line). (Note that the GLOSSAC aerosol data only extends until 2018). In (b) and (c), the IEFDH all perturbations temperature change from (a) is plotted again as the thick pale pink line. See the main text for further details of the radiative calculation.

Following the water vapour drop in 2000, temperatures in ERA5 from 2001 to 2005 (30° N – S average) are found to be 0.46 K lower than the average from 1996 to 2000 at 70 hPa. The IEFDH calculation with all the perturbations gives a corresponding temperature change of -0.46 K at 70 hPa of which -0.42 K comes from a reduction in ozone, -0.34 K from dynamical cooling while water vapour changes led to a warming of 0.26 K. The small remainder can be attributed to changes in aerosols and carbon dioxide.

At the cold point near 90 hPa (Figure S4), temperatures in ERA changed by -0.36 K. Here again ozone dominated the signal, contributing a cooling (-0.34 K). Dynamical cooling led to a further -0.23 K change, while water vapour changes contributed a warming of 0.2 K. The relatively larger radiative role for water vapour near the cold point has been noted by other studies (Ming et al., 2017).

Other water vapour drops have been reported in 2011/2012 (Urban et al., 2014) and again in 2016 (Avery et al., 2017; Diallo et al., 2018). Temperatures increased during the 2011/2012 water vapour drop and decreased during the 2016 drop but in neither

case were the changes as persistent as those that followed 2000 and we do not attempt to quantify the contribution from the different perturbations.

4.3 Volcanic eruptions

Volcanic eruptions release sulphate aerosol into the tropical lower stratosphere which leads to local heating (Stenchikov et al., 1998) and increased upwelling (Poberaj et al., 2011). During the time period considered here, the largest eruption that affected the temperature was the tropical Pinatubo volcanic eruption on 15 June 1991. The aerosol effect is represented by changing the optical depth in the IEFDH calculation. The aerosol heating leads to a maximum temperature increase of 3.3 K about 6 months after the eruption whilst the dynamical cooling produces a maximum decrease in temperature of 2 K (Figure 2(c)). Model studies show that the Pinatubo eruption leads to a decrease in ozone arising from both dynamics and chemistry (e.g., Kilian et al., 2020; Ming et al., 2020). In the IEFDH calculation, the ozone and dynamical temperature changes do not appear to be correlated during the eruption. However, there are large uncertainties in the ozone changes during the eruption. In the first 6 months following the eruption, a large number of ozone and water profiles below 20 hPa are filtered out of the satellite datasets due to poor retrieval quality in an opaque atmosphere. Nevertheless, the IEFDH calculation shows good agreement with the ERA5 temperature perturbation at 70 hPa in the three years following the Pinatubo eruption.

Other smaller volcanic eruptions affected the temperature during this time period. The Nevado del Ruiz eruption in 1986 (Vernier et al., 2011) contributed 0.4 K at the peak and several smaller tropical eruptions after the year 2000 contribute to transient perturbations of less than 0.1 K each.

4.4 Carbon dioxide

Carbon dioxide in the stratosphere leads to cooling. The increase in carbon dioxide concentrations adds a linear increase in the temperature of 0.2 K between 1984 and 2020. This linear trend is shown in Figure 2(c). The increase in temperature in the lower stratosphere is expected from an increase in CO₂ since the increased shortwave absorption dominates in the region below 40 hPa (see for e.g., Wang & Huang, 2020, for a detailed discussion). Appendix B contains more details of the vertical profile of the CO₂ induced temperature change.

5 QBO contributions

In Figure 1, a clear downward propagating QBO pattern is visible in the temperature in both plots. The contribution of the ozone changes associated with the QBO to the temperature variability will now be quantified using the IEFDH calculation. As discussed in the introduction, the secondary circulations associated with eastward and westward shear zones produce ozone anomalies. The ozone variability associated with the QBO is obtained by identifying the Principal Oscillation Patterns (POP) (von Storch & Zwiers, 2002; Xu, 1992) and associated timeseries from the ozone data (see also Figure S5). The calculation uses a similar method to Sheshadri and Plumb (2017), who use the POP method to study the mid-latitude jet, but is applied to zonal wind and ozone with the seasonal cycle and linear trend removed. The main POP is complex and similar to the linear combination of the first two empirical orthogonal functions of the respective fields. The structure of this POP is shown in Appendix C.

The QBO is confined to a narrow equatorial region and we focus on the average of 10° N – S in this section. Figure 3(a) shows the change due to the full ozone field and from the QBO at 70 hPa. The QBO only contributes to about ± 1.0 K to the temperature variability which is consistent with previous work on this topic (Li et al., 1995).

The corresponding contribution at 90 hPa is about ± 0.9 K (Figure S6). Figures 3(b) and (c) show the vertical structure of the temperature changes from the full ozone field and from the leading ozone POP timeseries respectively and figure 3(d) shows the difference between (b) and (c). The QBO contributes to a larger part of the variability in ozone above 40 hPa than below. Part of this variability shown in Figure 3(d) will be described by other POPs (not included in this analysis) that also correspond to QBO-related variability with a slightly different timescale to the main POP. Nonetheless, there are clear periods where the behaviour is not QBO-like. For instance, during 1991 Pinatubo eruption, there is a dipole structure in the temperature change due to ozone which descends over the course of 1993. This arises from a decrease in ozone in the lower stratosphere which causes the decreases in temperature. The longwave radiation that is not absorbed in this region is then absorbed further up to give the increase in temperature. During the water vapour drops in 2000 and 2010, there are further non-QBO ozone contribution although the two events are very different in character. There is a prolonged temperature increase due to ozone during 2000 before the water vapour drop whilst the temperature increase happens after the water vapour drop in 2011. The 2016 water vapour drop is difficult to analyse since any ozone signal from it is obscured by the QBO 2016 disruption. This disruption event also has a descending dipole signature and will be analysed in more detail below in section 5.1. Finally, there is a prominent large and deep negative difference seen in 2003 which is of unknown origin.

5.1 QBO 2016 disruption

The QBO 2016 disruption (Osprey et al., 2016) was an unusual phenomenon where a shallow westward jet formed in the eastward phase of the QBO in the lower stratosphere between 40 to 100 hPa, as can be seen in Figure 4(a). The anomalous shear zones above and below this shallow westward jet are also associated with secondary circulations, similarly to the standard QBO shear zones, and give rise to large ozone anomalies. This disruption differs from the regular QBO. It is characterised by a strong jet appearing lower in the stratosphere and has a shorter vertical scale.

Ozone anomalies during this period are shown in Figure 4(d) and the corresponding IEFDH temperature change in Figure 4(g). Using the POP analysis, we generate a timeseries corresponding to the leading POP for the zonal wind (Figure 4(b)) and ozone (Figure 4(e)). The ozone POP time series is the same as that used in the calculations above in Figure 3 (see also Figure S5). This can be thought of as the time series associated with the regular 28 month oscillation and will not fully capture the disruption as shown in the difference in zonal wind in Figure 4(c) where the shallower vertical scale of the disruption can be seen. The ozone field in the POP is also positive, corresponding to relative descent associated with the eastward shear zone that was expected to descend from the mid stratosphere during this period (Figure 4c). The ozone changes during the QBO disruption in Figure 4(f) are consistent with those seen by Tweedy et al. (2017), who calculate the trace gas changes as the difference from a QBO composite. The IEFDH calculation in Figure 4(h) shows that the regular QBO would have contributed a broad positive temperature change in the vertical with a magnitude of about 1 K around 70 hPa in the absence of a disruption. Note that although the ozone perturbations in Figure 4(e) maximise around 30 hPa, the temperature change due to the ozone maximises lower down a combination of the steep vertical gradient in ozone in this region and the fact that radiative damping timescales maximise in a deep region around the cold point (Ming et al., 2017).

The effect of the QBO disruption on the ozone field is thus substantial and appears as a decrease between 40 to 100 hPa from Jan to Jun 2016 (Figure 4(f)). There is a corresponding decrease in temperature that extends down below the cold point with a maximum of about 3 K at 70 hPa and an increase in temperature in the region above. This is consistent with reduced local absorption of upwelling longwave radiation where ozone

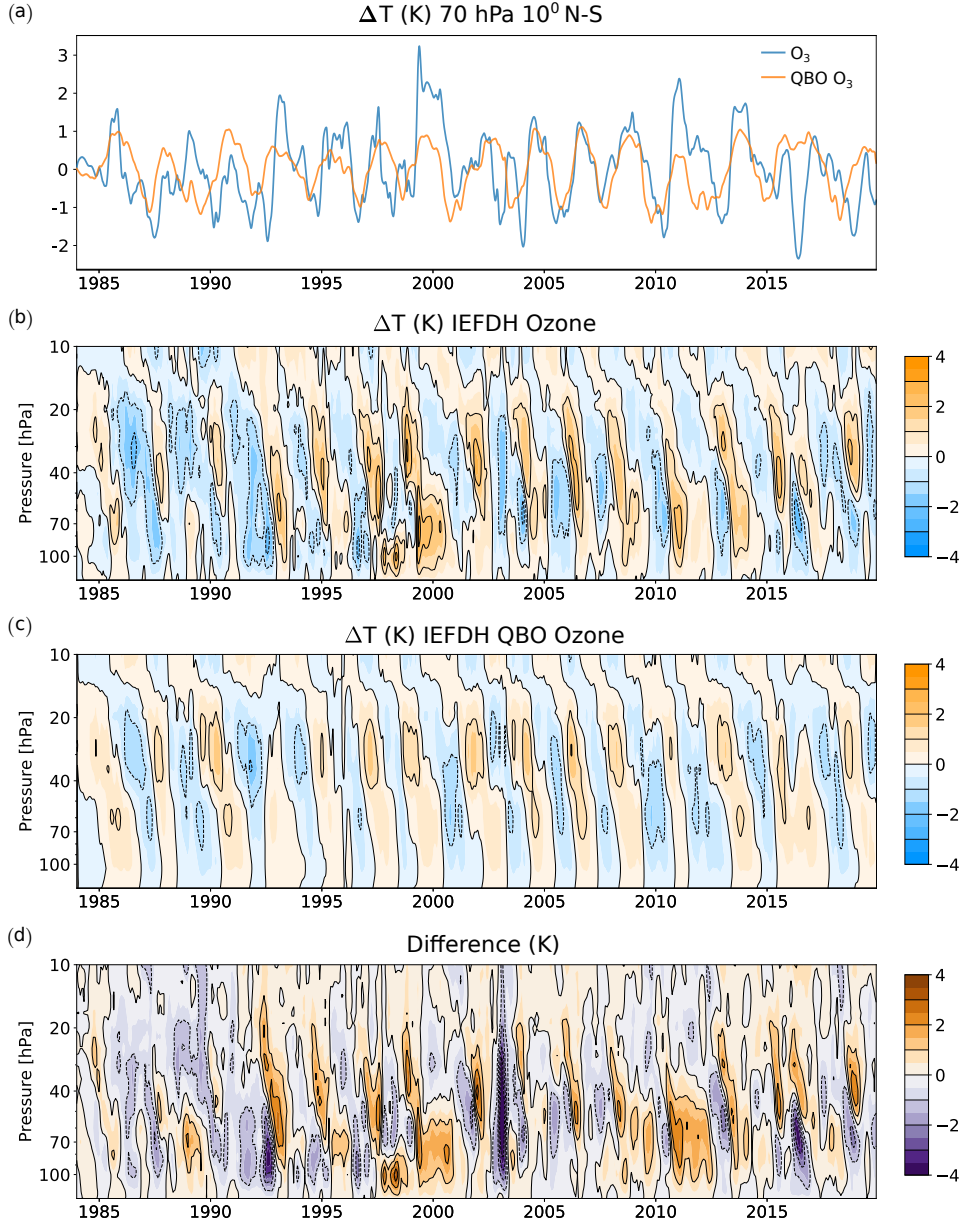


Figure 3. IEFDH temperature change (K), averaged between 10° N – S, from interannual variability in ozone and from the time series associated to the leading QBO ozone principal oscillation pattern. (a) Changes at 70 hPa. Pressure-time plots of the (b) ozone contribution (c) the QBO ozone contribution. (d) The difference between (b) and (c).

is low and increased absorption above the ozone perturbation. This is substantially larger than the ozone-related temperature changes associated with typical QBO variability.

Comparing the ozone and the dynamical contributions in the wider 30° N – S region (Figures 2(a) and (b)), we speculate that the ozone temperature contribution arising from the QBO disruption is the dominant effect and that the ERA5 upwelling is poorly represented during 2016. This results in the IEFDH calculation overestimating the total temperature change by about 1.5 K compared to ERA5. Note that there is also a stronger

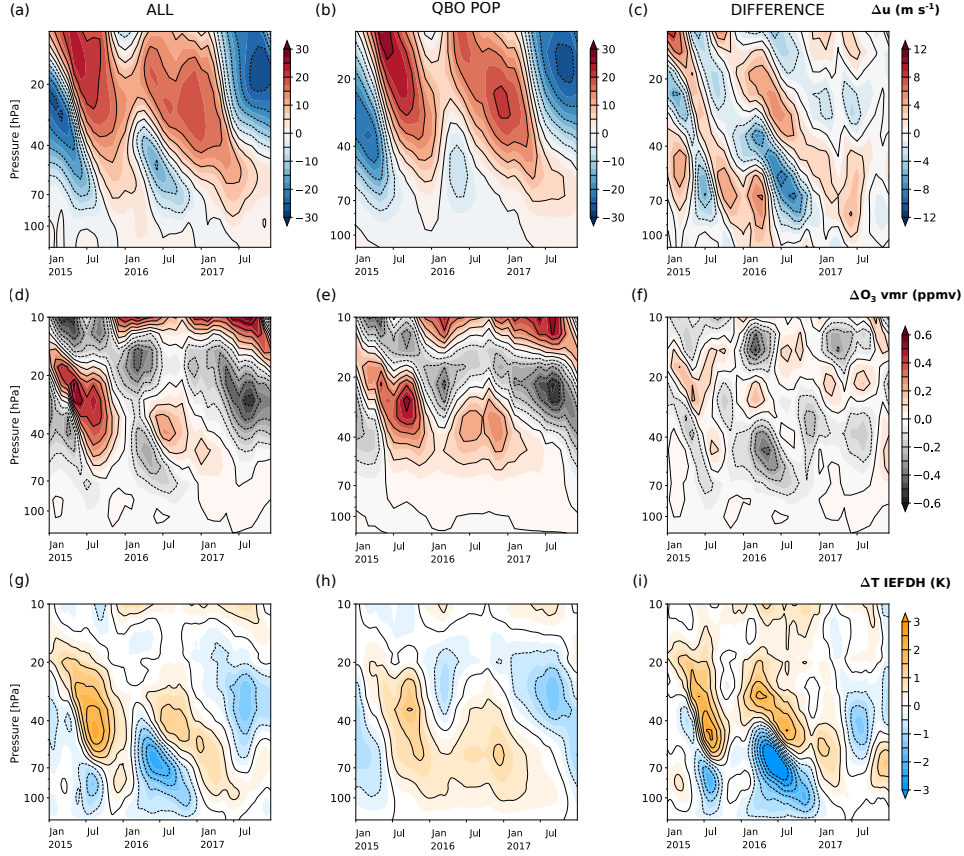


Figure 4. The grid shows the changes in zonal wind (first row), ozone (second row) and temperature from the IEFDH calculation (third row) during the QBO 2016 disruption. All quantities are averaged between 10° N – S. In the first column, the full interannual variability (ALL) in zonal wind is shown in (a) and for ozone in (d). The seasonal cycle and trends have been removed. (d) shows the corresponding IEFDH temperature change from the ozone perturbation in (g). In the second column, the QBO component has been identified (QBO POP) as the time series corresponding to the leading POP for the zonal wind in (b) and the leading POP in ozone in (e). The corresponding IEFDH temperature change to (e) is shown in (h). The figures (c), (f) and (i) in third column show the difference between corresponding figures from the first column and the second column (ALL minus QBO POP). The second and third rows of figures share the same colourbar.

downward trend in the calculated IEFDH temperatures compared to ERA5 from 2016 onward which complicates this analysis.

The QBO 2016 disruption provides an interesting case study to test the robustness of QBO-related processes in global models. The temperature change resulting from the ozone perturbations will depend strongly on correctly simulating the radiative changes and the secondary meridional circulation. It is not guaranteed that a model that captures the main zonal wind disruption will capture the details of the processes that lead to the corresponding ozone changes.

6 Quantifying the ozone radiative feedback

We have shown that ozone changes are an important contributor to the temperature interannual variability. We now consider ways to quantify this radiative effect. First it is informative to look at the lagged correlation, calculated at each pressure level, between pairs of ERA5 temperature, dynamical heating and ozone. The Pearson correlation coefficient is shown in Figure 5 and significance is calculated using a non-parametric test which randomises the phases of the input time series following Ebisuzaki (1997). We include the lagged correlation between ERA5 temperature and water vapour for completeness and will only discuss those briefly since the correlations are low and less important than ozone.

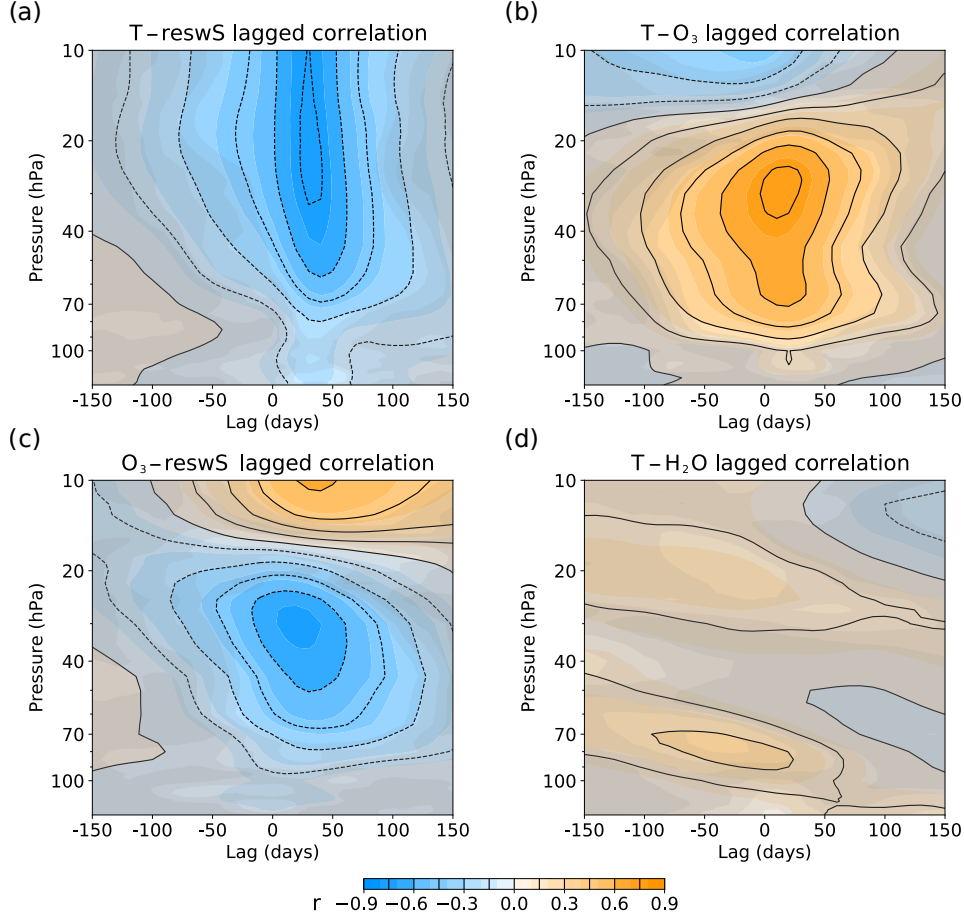


Figure 5. Time (lag) vs. height sections created by regressing monthly time series (1995 to 2019) of (a) temperature versus $\bar{w}^* \bar{S}$, (b) temperature versus ozone, (c) ozone versus $\bar{w}^* \bar{S}$ and (d) temperature versus water vapour at different levels and time lags. Positive lags indicate that the first quantity lags behind the second. The grey fog which is plotted as overlaid contours with different levels of transparency represents confidence levels of 95, 90, 80, 70 and 60% using a non-parametric test which randomises the phases of the input time series following Ebisuzaki (1997).

Figure 5(a) shows a large negative correlation between temperature and the upwelling term ($-Q_{\text{dyn}}$). The correlation is strongest at 20 hPa and decreases lower down towards 70 hPa. At 70 hPa, the correlation peaks around 40 days and decreases to about

30 days at 10 hPa. This is consistent with increased upwelling leading to dynamical cooling and a lagged radiative response in the temperature with radiative time scales decreasing with altitude. Ozone is positively correlated with temperature on a broad range of timescales (Figure 5(b)) with the correlation maximising at a lag of around 20 days below 20 hPa. Above this region, the photochemistry of ozone becomes important. Below this region, ozone can be regarded as a passive tracer that is affected by transport. Note that temperatures are more highly correlated with ozone than with the dynamical heating around 70 hPa (Figure 5(a)). The vertical transport of ozone leads to the structures seen in Figure 5(c) where an increase in upwelling draws up more ozone poor air, from the troposphere below, into the stratosphere and leads to a decrease in ozone. The largest correlation occurs at 30 hPa at a lag of 20 days. At 70 hPa, these correlations maximise around 40 days. These plots show that as upwelling increases, the temperature decreases due to both the dynamical heating change and the ozone decreases as a result of the vertical transport. Hence, there is an important enhancement of the temperature response to the dynamical heating that comes from the ozone-transport feedback. This can alternatively be thought of as a smaller upwelling being required to maintain a given temperature.

We note that there is an interesting structure in the temperature water vapour lagged correlation in Figure 5(d) with a positive lagged correlation starting around the cold point and extending upwards and backwards in lag. Water vapour at the cold point is correlated with the temperature at that level and the resulting tape recorder signal in water vapour is advected upwards. Hence the water vapour at any level, and its subsequent temperature effect, is correlated with the water vapour at the cold point (with a lag determined by the speed of the upward transport). Temperatures at different levels are also correlated to each other due to the non-local effects of radiation. These complex non-local interactions lead to the structures seen.

We now quantify the changes in radiative damping rates as follows. We take the difference between Equations 2 and 3 and split the longwave (LW) heating rate change into the component arising from the temperature change only, $-\alpha_T \Delta\bar{T}$, and other radiative terms, \bar{A}_1 , as in Equation 4.

$$\begin{aligned} \partial_t \Delta\bar{T} - \Delta\bar{Q}_{\text{dyn}} &= Q_{\text{LW}}(\bar{\chi}^0, \bar{T}) - Q_{\text{LW}}(\bar{\chi}^0, \bar{T}^0) + \bar{A} \\ &= -\alpha_T \Delta\bar{T} + \bar{A}_1 \end{aligned} \quad (4)$$

Since ozone is correlated with temperature (Figure 5(b)), we could also split the right hand side into longwave (LW) heating terms due to changes in ozone and temperature and other radiative terms (\bar{A}_2). We also assume that the changes in longwave heating can be written as linear damping term ($-\alpha\Delta\bar{T}$) as in Equation 6.

$$\partial_t \Delta\bar{T} - \Delta\bar{Q}_{\text{dyn}} = Q_{\text{LW}}(\bar{O}_3, \bar{T}) - Q_{\text{LW}}(\bar{O}_3^0, \bar{T}^0) + \bar{A}_1 \quad (5)$$

$$= -\alpha \Delta\bar{T} + \bar{A}_2 \quad (6)$$

We run the radiative code to extract the relevant longwave heating rates when prescribing ERA5 temperature interannual variations (\bar{T}). The various damping rates are calculated using linear regression, at every pressure level and latitude, between the heating rates and ERA5 temperatures. The damping timescales, $\tau = 1/\alpha$, and damping rates, α are shown in Figure 6(a) and (b) respectively and Figure 6(c) shows the fraction of the variance explained. The latitudinal variation in α and the explained variance is shown in Figure S7.

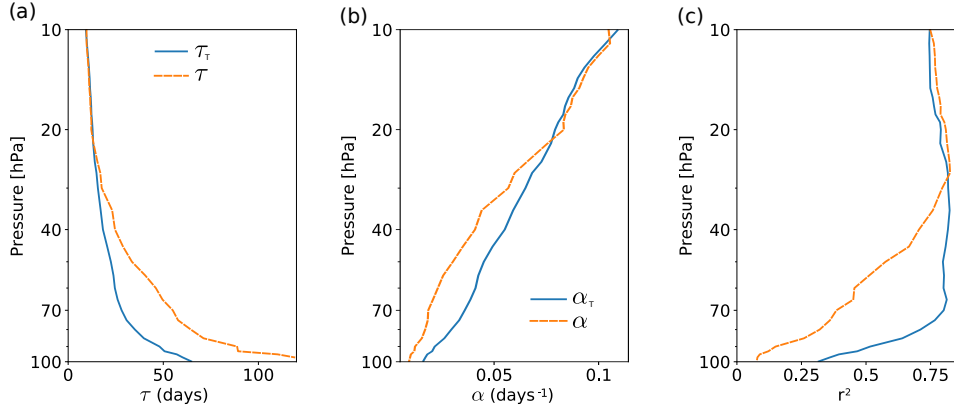


Figure 6. Radiative damping (a) timescales and (b) rates calculated using linear regression of heating rates derived from the radiation code against ERA5 temperatures. The solid blue line shows the regression using longwave heating rate changes from temperature only and the dashed orange line uses longwave heating rate changes from temperature and ozone changes. The fraction of variance in longwave heating rates explained by local temperature anomalies is shown in (c). All values are averaged between 30° N – S.

The solid blue line in Figure 6(a) shows that the radiative timescale, $1/\alpha_T$, is about 29 days around 70 hPa, increasing to 49 days around 90 hPa. Longwave radiative damping rates are dominated by CO₂ and are dependent on temperature (e.g., Fels, 1982; Newman & Rosenfield, 1997; Hitchcock et al., 2010). Temperature changes explain most of the variance in longwave radiative damping rates ($r^2 > 0.7$ above 70 hPa).

If we including the ozone changes in the longwave heating rates ($1/\alpha$, dashed orange line), as given by Equation 6, the additional correlation between ozone and temperatures leads to a timescale of ~ 55 days at 70 hPa to ~ 88 days at 90 hPa (dashed orange line) although the fraction of the variance explained falls rapidly below 40 hPa. These longer timescales are consistent with the value of 70 days obtained by Fueglistaler et al. (2014).

Alternatively, it is more physically relevant to think of the ozone only radiative heating as an enhancement of the dynamical heating since it arises from the transport of ozone by the upwelling. Hence we can also write Equation 5 above as:

$$\begin{aligned} \partial_t \Delta \bar{T} - \Delta \bar{Q}_{\text{dyn}} &= Q(\bar{O}_3, \bar{T}^0) - Q(\bar{O}_3^0, \bar{T}^0) - \alpha_T \Delta \bar{T} + \bar{A}_2 \\ \partial_t \Delta \bar{T} - (1 + \beta) \Delta \bar{Q}_{\text{dyn}} &= -\alpha_T \Delta \bar{T} + \bar{A}_2 \end{aligned} \quad (7)$$

where β represents the enhancement of the radiative effect of the dynamical heating due to the ozone transport and \bar{A}_2 includes all other radiative terms. Note that, we are considering the change in longwave and shortwave heating rates due to ozone in this case. The enhancement in dynamical heating, β , is calculated by linear regression between the ozone only heating rate and the dynamical heating and is shown in Figure 7.

Figure 7(a) shows that we can think of the ozone-transport effect as enhancing the dynamical heating term as in Equation 7. The increase is substantial and of about 20% at 70 hPa and peaking at 40% at 35 hPa. The additional radiative effect of the vertical transport of ozone translates into a smaller upwelling being required to cause the same temperature change. The quality of the fit is poor for the 30° N – S average, as shown by Figure 7(b) but improves in the region 10° N – S (see Figure S8) which could be due to a better correlation between upwelling and ozone within the latitude range where the

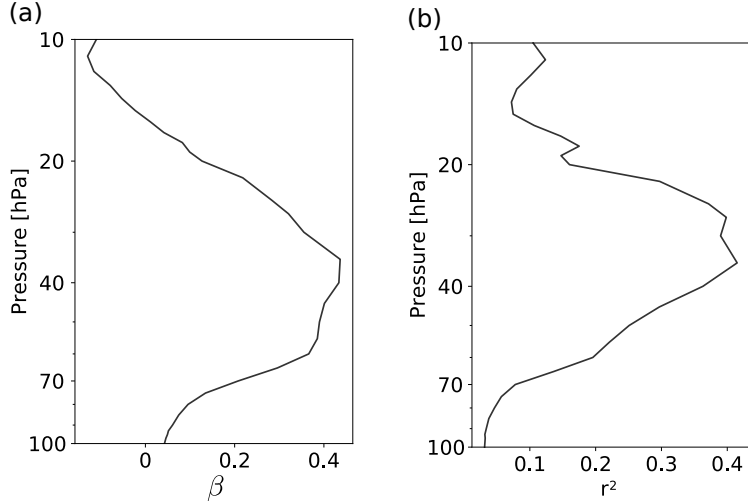


Figure 7. (a) Enhancement of dynamical heating due to ozone transport radiative feedback calculated using linear regression of heating rate arising from ozone only against the dynamical heating. (b). The fraction of variance explained the linear regression. All values are averaged between 30° N – S.

QBO has a strong influence. We also note that the results in Figure 7(a) are not consistent with those in Figure 6; values of β are smaller than what would be expected from the changes in α . Ozone is more strongly correlated with temperatures below 40 hPa than with the dynamical heating as seen in Figure 5(b) and (c). This could be due to other processes contributing to ozone changes other than upwelling in this region.

7 Discussion

We have shown that it is possible to reproduce the interannual variability in lower stratospheric temperatures using a 1D radiative calculation and such a calculation allows us to decompose the temperature changes into various components. We apply various continuous perturbations and use the radiative code is used to calculate the change in heating rate which is then used to update the temperature. This interannually evolving fixed dynamical heating calculation (IEFDH) calculation is an extension of a similar calculation used for seasonal cycle changes (Forster et al., 2007). By calculating the temperature change using this new technique, we are able quantify the contribution from dynamical heating, ozone, water vapour, aerosol and the linear trend in carbon dioxide.

We have shown that at 70 hPa, the ± 3 K interannual changes in temperature can primarily be explained by variations in dynamical heating (up to ± 2.1 K) and variations in ozone (up to ± 1.6 K). A smaller contribution (up to ± 0.4 K) arises from water vapour changes. Aerosol changes and the linear trend in carbon dioxide make up most of the remaining variability. The contributions from aerosols dominate the time series during the 1991 Pinatubo volcanic eruption, with changes up to 3.3 K at the peak, a few months after the eruption. Carbon dioxide adds a linear warming of about 0.2 K over the time period from 1984 to 2019.

This calculation emphasises the substantial role of ozone in contributing to the interannual variability in temperature. In the lower stratosphere, the ozone budget is dominated by transport and increases in upwelling act to decrease ozone. This feedback amplifies the temperature response of a change in upwelling. Temperature changes are positively correlated to ozone change and negatively correlated to the upwelling. The trans-

port feedback means that for a given change in upwelling, the additional changes in ozone result in a larger temperature change than would be expected simply from the change in dynamical heating. This can also be thought of as a smaller change in upwelling being required to achieve the same temperature change or as an increase in the radiative damping time scale. We have quantified using the radiative code and find including the ozone correlation with temperature changes the radiative damping time scale by 50% at 70 hPa to about 56 days. If, instead, we view the ozone changes as primarily arising from changes in upwelling, this transport effect enhances the dynamical heating term by 20% at 70 hPa and peaking at 40% at 35 hPa. We find that these two approaches do not yield similar results since the ozone-temperature correlation is stronger than the ozone-upwelling correlation.

A component of the ozone variability related to the quasi-biennial oscillation (QBO) is extracted using a principal oscillation pattern analysis (POP). The time series that corresponds to the leading POP is used to calculate the QBO induced ozone temperature change in the IEFDH calculation. This corresponds to a temperature change of about ± 1 K at 70 hPa. We also find a substantial amount of non-QBO variability, especially in the region below 40 hPa. This is particularly visible around the Pinatubo volcanic eruption, and around the years 2000 and 2011 which coincide with previously reported water vapour drop events.

The POP analysis also allowed us to look in more detail at the unusual QBO disruption in 2016 during which a shallow westward jet formed within the eastward phase of the QBO in the lower stratosphere. Assuming the QBO POP timeseries represents the “regular” QBO, we can obtain the anomalous ozone change during the disruption and calculate the corresponding IEFDH temperature change. If 2016 were a regular QBO year, we would have expected ozone to contribute to warming in the region below 40 hPa. Instead, the ozone change arising from the disruption leads to a dipole structure around 40 hPa with a maximum cooling of 3 K at 70 hPa and a warming above with a maximum of 2 K at 30 hPa. This dipole structure follows the descending wind shear associated with the disruption. Together with the change in temperature from dynamical heating, the QBO 2016 disruption caused a large anomaly in the temperature comparable to the Pinatubo volcanic eruption.

The IEFDH calculation also shows that water vapour changes are a secondary contributor to the temperature change (about ± 0.3 K at 70 hPa). The increase in carbon dioxide is assumed to be linear and adds a linear increase of 0.2 K between 1984 and 2019. The smaller volcanic eruptions, after the year 2000, do not have a significant effect on temperatures (less than 0.1 K at the peak).

The IEFDH calculation shows that it is possible to attribute the interannual changes in temperature to specific factors with reasonable accuracy and opens the possibility of more detailed studies into the feedbacks between dynamics and radiation. Ozone changes are large and enhance dynamical changes via the transport coupling. This effect will not be captured, for instance, by climate models using an ozone climatology. Furthermore, we have shown that the QBO 2016 disruption provides both an interesting case study and a test of the internally generated QBO in a climate model. To be able to capture the correct temperature change relies on the model accurately simulating the changes to waves, the accompanying ozone transport changes and the subsequent radiative impact on the dynamics.

Appendix A Correlation between IEFDH and ERA5 temperatures

Figure A1 shows the square of the correlation coefficient, r^2 , between the IEFDH calculation and ERA5 temperature data shown in Figure 1 for the time period 1984 to

1991 in (a) and 1992 to 2019 in (b). There is a strong correlation between the time series above 70 hPa and poorer agreement below 70 hPa.

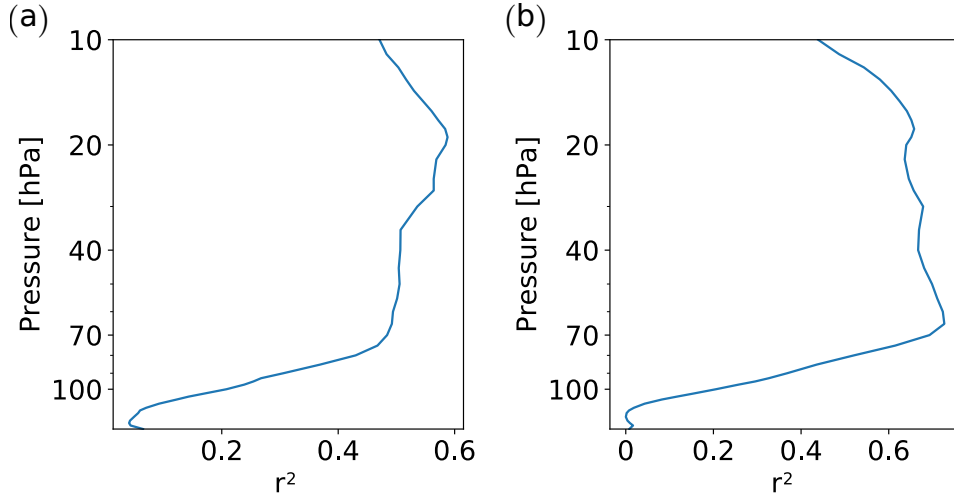


Figure A1. Correlation coefficient, r^2 , at different pressure levels between the 30° N – S average of the temperature in the IEFDH calculation and in ERA5 temperature. The time series is split into two sections: (a) 1984 to 1991 and (b) 1992 to 2019.

Appendix B CO₂ linear trend

The vertical profile of the temperature change between 2019 and 1984 due to the CO₂ linear trend is shown in Figure B1. CO₂ has been assumed to be well mixed and to be increasing linearly from 345 ppmv (1984 value) to 412 ppmv (2019 value). Carbon dioxide is the dominant emitter in the stratosphere and increasing carbon dioxide leads to increases cooling throughout most of the stratosphere from the increase in long-wave emission. In the tropical lower stratospheric region (30 hPa and below), the long-wave emission is small and the shortwave heating dominates causing the temperature increase seen. This is only the case over the latitude range where there is high solar insolation: 30° N – S on average and shifting with season. Our results are consistent with those of Wang and Huang (2020) but the vertical extent of the warming is somewhat broader and results in Huang and Wang (2019) suggest that there are temperature biases in the predicted response from different radiation codes.

Appendix C principal Oscillation Patterns (POP)

We extract the QBO variability in zonal mean zonal wind and zonal mean ozone using principal oscillation pattern analysis following the method in Sheshadri and Plumb (2017). We use data between 20° N – S and 10 to 1000 hPa. The seasonal cycle and linear trends are removed before the POP analysis. For computational efficiency, the process is done in empirical orthogonal function (EOF) space and requires choosing a lag for the principal component lag covariances. We do not truncate the EOFs and choose a lag of 9 months for the zonal wind and 12 months for ozone. Vertical pressure weighting, as used in Sheshadri and Plumb (2017) does not substantially affect this calculation and we do not weight the fields. Using the various methods in Gallagher et al. (1991), we check that leading POP obtained is sensible. Choosing a different lag, provided it is long enough, will yield a slightly different leading POPs but with very similar spatial patterns. We tested lags between 9 to 14 months and simply choose the lag where the lead-

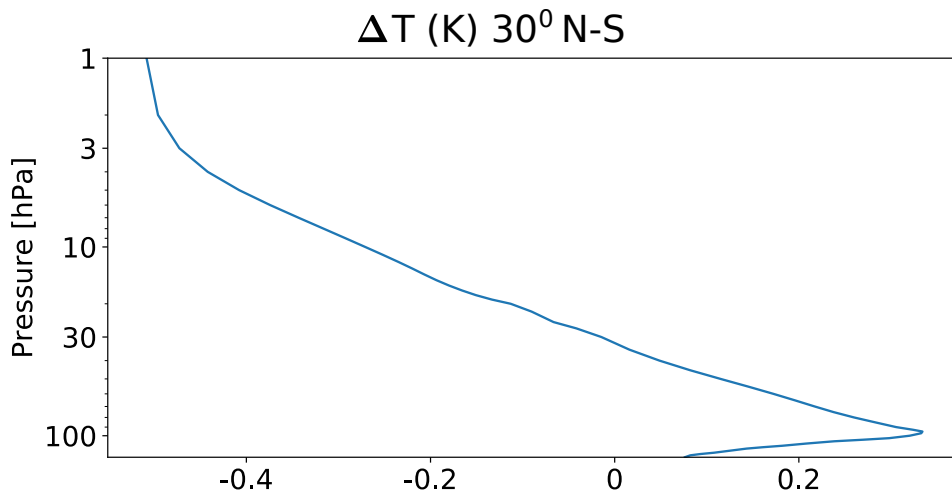


Figure B1. Difference in temperature, calculated from the radiative calculation, between 2019 and 1984 due to the CO₂ linear trend. The values are averaged between 30° N – S.

ing POP explained most of the variance. For the zonal wind, the real and imaginary parts of the leading POP which explains 47% of the variance is shown in Figures C1(a) and (b). These are very similar to the leading EOFs (Figures C1(c) and (d)) which adds confidence to the analysis. The leading POP has a decay timescale of 71.8 months and an oscillation timescale of 28.2 months. For ozone, leading POP (explaining 30% of the variance) has a decay timescale of 97.9 months and an oscillation timescale of 27.6 months.

We construct the zonal wind and the ozone timeseries that corresponds to the leading QBO POPs in each by first calculating the principal adjoint patterns and taking the scalar product of the field with the principal adjoint pattern.

Acknowledgments

AM would like to acknowledge support from the Leverhulme Trust as an early career fellow. We thanks Aditi Sheshadri, Alan Plumb, Stephan Fueglistaler and Peter Haynes for discussions that greatly improved the manuscript.

Data availability

SWOOSH data can be downloaded from <https://csl.noaa.gov/groups/csl8/swoosh/>. The ERA and ERA5.1 datasets were obtained from the Copernicus Climate Change Service at <https://cds.climate.copernicus.eu/>. The GLOSSAC V2.0 data was obtained from <https://asdc.larc.nasa.gov/project/GloSSAC/GloSSAC.2.0>

References

- Andrews, D. G., Holton, J. R., & Leovy, C. B. (1987). *Middle atmosphere dynamics*. Academic Press, Orlando.
- Avery, M., Davis, S., Rosenlof, K., Ye, H., & Dessler, A. (2017, 05). Large anomalies in lower stratospheric water vapour and ice during the 2015–2016 el niño. *Nature Geoscience, advance online*, tbd. doi: 10.1038/ngeo2961
- Brinkop, S., Dameris, M., Jöckel, P., Garny, H., Lossow, S., & Stiller, G. (2016). The millennium water vapour drop in chemistry–climate model simulations. *Atmospheric Chemistry and Physics*, 16(13), 8125–8140. doi: 10.5194/acp-16-8125-2016

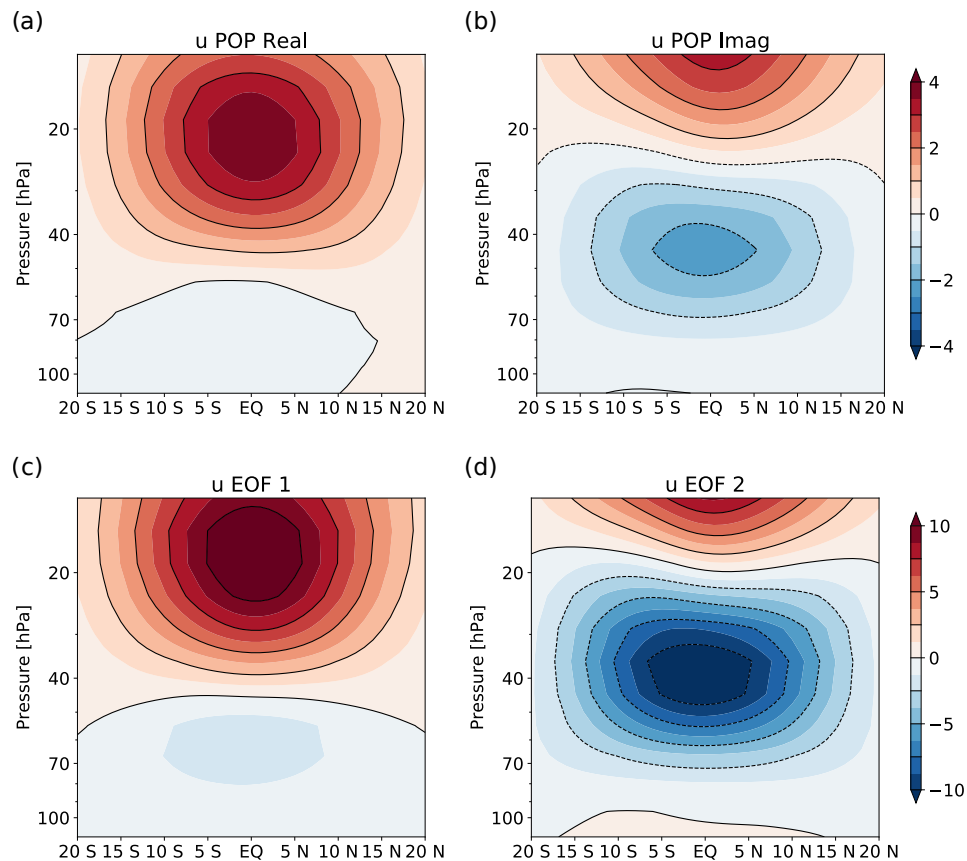


Figure C1. (a) Real and (b) imaginary components of the leading principal Oscillation Pattern calculated from the deseasonalised and detrended ERA5 zonal mean zonal wind. (c) First and (d) second Empirical Orthogonal functions for comparison. Rows of plots share the same colourbars.

- (C3S), C. C. C. S. (2017). *Era5: Fifth generation of ecmwf atmospheric reanalyses of the global climate*. Copernicus Climate Change Service Climate Data Store (CDS), Date of access: Sept 2020. Retrieved from <https://cds.climate.copernicus.eu> doi: 10.5065/D6X34W69
- Charlesworth, E. J., Birner, T., & Albers, J. R. (2019). Ozone transport-radiation feedbacks in the tropical tropopause layer. *Geophysical Research Letters*, *46*(23), 14195–14202. doi: <https://doi.org/10.1029/2019GL084679>
- Davis, S. M., Rosenlof, K. H., Hassler, B., Hurst, D. F., Read, W. G., Vömel, H., ... Damadeo, R. (2016). The stratospheric water and ozone satellite homogenized (swoosh) database: a long-term database for climate studies. *Earth System Science Data*, *8*(2), 461–490. doi: 10.5194/essd-8-461-2016
- Dhomse, S., Weber, M., & Burrows, J. (2008). The relationship between tropospheric wave forcing and tropical lower stratospheric water vapor. *Atmospheric Chemistry and Physics*, *8*(3), 471–480. doi: 10.5194/acp-8-471-2008
- Diallo, M., Riese, M., Birner, T., Konopka, P., Müller, R., Hegglin, M. I., ... Ploeger, F. (2018). Response of stratospheric water vapor and ozone to the unusual timing of el niño and the qbo disruption in 2015–2016. *Atmospheric Chemistry and Physics*, *18*(17), 13055–13073. doi: 10.5194/acp-18-13055-2018
- Ebisuzaki, W. (1997). A method to estimate the statistical significance of a corre-

- lation when the data are serially correlated. *Journal of Climate*, *10*(9), 2147 - 2153. doi: 10.1175/1520-0442(1997)010<2147:AMTETS>2.0.CO;2
- Fels, S. (1982). A parameterization of scale-dependent radiative damping rates in the middle atmosphere. *Journal of the Atmospheric Sciences*, *39*, 1141-1152. doi: [https://doi.org/10.1175/1520-0469\(1982\)039<1141:APOSDR>2.0.CO;2](https://doi.org/10.1175/1520-0469(1982)039<1141:APOSDR>2.0.CO;2)
- Forster, P. M., Bodeker, G., Schofield, R., Solomon, S., & Thompson, D. (2007). Effects of ozone cooling in the tropical lower stratosphere and upper troposphere. *Geophysical Research Letters*, *34*(23), 1–5. doi: 10.1029/2007GL031994
- Fueglistaler, S., Abalos, M., Flannaghan, T. J., Lin, P., & Rande, W. J. (2014). Variability and trends in dynamical forcing of tropical lower stratospheric temperatures. *Atmospheric Chemistry and Physics*, *14*(24), 13439–13453. doi: 10.5194/acp-14-13439-2014
- Gallagher, F., von Storch, H., Schnur, R., & Hannoschöck, G. (1991). *The pop manual*. (Tech. Rep.). Deutsches Klimarechenzentrum. Retrieved from <http://www.hvonnstorch.de/klima/pdf/POP-manual.dkrz.1991.pdf>
- Garfinkel, C. I., Gordon, A., Oman, L. D., Li, F., Davis, S., & Pawson, S. (2018). Nonlinear response of tropical lower-stratospheric temperature and water vapor to ENSO. *Atmospheric Chemistry and Physics*, *18*(7), 4597–4615. doi: 10.5194/acp-18-4597-2018
- Gilford, D., & Solomon, S. (2017). Radiative effects of stratospheric seasonal cycles in the tropical upper troposphere and lower stratosphere. *Journal of Climate*, *30*(8), 2769 - 2783. doi: 10.1175/JCLI-D-16-0633.1
- Gilford, D., Solomon, S., & Portmann, R. (2016, 10). Radiative impacts of the 2011 abrupt drops in water vapor and ozone in the tropical tropopause layer. *Journal of Climate*, *29*, 151029140234000. doi: 10.1175/JCLI-D-15-0167.1
- Hersbach, H., Bell, B., Berrisford, P., Hirahara, S., Horányi, A., Muñoz-Sabater, J., ... Thépaut, J.-N. (2020). The ERA5 global reanalysis. *Quarterly Journal of the Royal Meteorological Society*, *146*(730), 1999-2049. doi: <https://doi.org/10.1002/qj.3803>
- Hitchcock, P., Shepherd, T. G., & Yoden, S. (2010). On the approximation of local and linear radiative damping in the middle atmosphere. *Journal of the Atmospheric Sciences*, *67*(6), 2070 - 2085. doi: 10.1175/2009JAS3286.1
- Huang, Y., & Wang, Y. (2019). How does radiation code accuracy matter? *Journal of Geophysical Research: Atmospheres*, *124*(20), 10742-10752. doi: <https://doi.org/10.1029/2019JD030296>
- Kilian, M., Brinkop, S., & Jöckel, P. (2020). Impact of the eruption of mt pinatubo on the chemical composition of the stratosphere. *Atmospheric Chemistry and Physics*, *20*(20), 11697–11715. doi: 10.5194/acp-20-11697-2020
- Kovilakam, M., Thomason, L. W., Ernest, N., Rieger, L., Bourassa, A., & Millán, L. (2020). The global space-based stratospheric aerosol climatology (version 2.0): 1979–2018. *Earth System Science Data*, *12*(4), 2607–2634. doi: 10.5194/essd-12-2607-2020
- Li, D., Shine, K. P., & Gray, L. J. (1995). The role of ozone-induced diabatic heating anomalies in the quasi-biennial oscillation. *Quarterly Journal of the Royal Meteorological Society*, *121*(524), 937-943. doi: <https://doi.org/10.1002/qj.49712152411>
- Maycock, A. C., Joshi, M. M., Shine, K. P., Davis, S. M., & Rosenlof, K. H. (2014). The potential impact of changes in lower stratospheric water vapour on stratospheric temperatures over the past 30 years. *Quarterly Journal of the Royal Meteorological Society*, *140*(684), 2176-2185. doi: <https://doi.org/10.1002/qj.2287>
- Ming, A., Maycock, A. C., Hitchcock, P., & Haynes, P. (2017). The radiative role of ozone and water vapour in the annual temperature cycle in the tropical tropopause layer. *Atmospheric Chemistry and Physics*, *17*(9), 5677–5701. doi: 10.5194/acp-17-5677-2017

- Ming, A., Winton, V. H. L., Keeble, J., Abraham, N. L., Dalvi, M. C., Griffiths, P., ... Yang, X. (2020). Stratospheric ozone changes from explosive tropical volcanoes: Modeling and ice core constraints. *Journal of Geophysical Research: Atmospheres*, *125*(11), e2019JD032290. doi: <https://doi.org/10.1029/2019JD032290>
- Mote, P. W., Holton, J. R., & Boville, B. A. (1994). Characteristics of stratosphere-troposphere exchange in a general circulation model. *Journal of Geophysical Research: Atmospheres*, *99*(D8), 16815-16829. doi: <https://doi.org/10.1029/94JD00913>
- NASA/LARC/SD/ASDC. (2018). *Global space-based stratospheric aerosol climatology version 2.0*. NASA Langley Atmospheric Science Data Center DAAC. doi: [10.5067/GLOSSAC-L3-V2.0](https://doi.org/10.5067/GLOSSAC-L3-V2.0)
- Newman, P. A., & Rosenfield, J. E. (1997). Stratospheric thermal damping times. *Geophysical Research Letters*, *24*(4), 433-436. doi: <https://doi.org/10.1029/96GL03720>
- Osprey, S. M., Butchart, N., Knight, J. R., Scaife, A. A., Hamilton, K., Anstey, J. A., ... Zhang, C. (2016). An unexpected disruption of the atmospheric quasi-biennial oscillation. *Science*, *353*(6306), 1424-1427. doi: [10.1126/science.aah4156](https://doi.org/10.1126/science.aah4156)
- Pahlavan, H. A., Fu, Q., Wallace, J. M., & Kiladis, G. N. (2021). Revisiting the quasi-biennial oscillation as seen in era5. part i: Description and momentum budget. *Journal of the Atmospheric Sciences*, *78*(3), 673 - 691. doi: [10.1175/JAS-D-20-0248.1](https://doi.org/10.1175/JAS-D-20-0248.1)
- Plumb, R. A., & Bell, R. C. (1982). A model of the quasi-biennial oscillation on an equatorial beta-plane. *Quarterly Journal of the Royal Meteorological Society*, *108*(456), 335-352. doi: <https://doi.org/10.1002/qj.49710845604>
- Poberaj, C. S., Staehelin, J., & Brunner, D. (2011). Missing stratospheric ozone decrease at southern hemisphere middle latitudes after mt. pinatubo: A dynamical perspective. *Journal of the Atmospheric Sciences*, *68*(9), 1922-1945. doi: [10.1175/JAS-D-10-05004.1](https://doi.org/10.1175/JAS-D-10-05004.1)
- Randel, W. J., Wu, F., Vömel, H., Nedoluha, G. E., & Forster, P. (2006). Decreases in stratospheric water vapor after 2001: Links to changes in the tropical tropopause and the brewer-dobson circulation. *Journal of Geophysical Research: Atmospheres*, *111*(D12). doi: <https://doi.org/10.1029/2005JD006744>
- Sheshadri, A., & Plumb, R. A. (2017). Propagating annular modes: Empirical orthogonal functions, principal oscillation patterns, and time scales. *Journal of the Atmospheric Sciences*, *74*(5), 1345 - 1361. doi: [10.1175/JAS-D-16-0291.1](https://doi.org/10.1175/JAS-D-16-0291.1)
- Stenchikov, G. L., Kirchner, I., Robock, A., Graf, H.-F., Antuña, J. C., Grainger, R. G., ... Thomason, L. (1998). Radiative forcing from the 1991 mount pinatubo volcanic eruption. *Journal of Geophysical Research: Atmospheres*, *103*(D12), 13837-13857. doi: <https://doi.org/10.1029/98JD00693>
- Tegtmeier, S., Anstey, J., Davis, S., Dragani, R., Harada, Y., Ivanciu, I., ... Wright, J. S. (2020). Temperature and tropopause characteristics from reanalyses data in the tropical tropopause layer. *Atmospheric Chemistry and Physics*, *20*(2), 753-770. doi: [10.5194/acp-20-753-2020](https://doi.org/10.5194/acp-20-753-2020)
- Thuburn, J., & Craig, G. C. (2002). On the temperature structure of the tropical stratosphere. *Journal of Geophysical Research*, *107*, 1-10.
- Tummon, F., Hassler, B., Harris, N. R. P., Staehelin, J., Steinbrecht, W., Anderson, J., ... Wild, J. (2015). Intercomparison of vertically resolved merged satellite ozone data sets: interannual variability and long-term trends. *Atmospheric Chemistry and Physics*, *15*(6), 3021-3043. doi: [10.5194/acp-15-3021-2015](https://doi.org/10.5194/acp-15-3021-2015)
- Tweedy, O. V., Kramarova, N. A., Strahan, S. E., Newman, P. A., Coy, L., Randel, W. J., ... Frith, S. M. (2017). Response of trace gases to the disrupted 2015-2016 quasi-biennial oscillation. *Atmospheric Chemistry and Physics*, *17*(11), 6813-6823. doi: [10.5194/acp-17-6813-2017](https://doi.org/10.5194/acp-17-6813-2017)

- Urban, J., Lossow, S., Stiller, G., & Read, W. (2014, 07). Another drop in water vapor. *Eos, Transactions American Geophysical Union*, 95. doi: 10.1002/2014EO270001
- Vernier, J.-P., Thomason, L. W., Pommereau, J.-P., Bourassa, A., Pelon, J., Garnier, A., ... Vargas, F. (2011). Major influence of tropical volcanic eruptions on the stratospheric aerosol layer during the last decade. *Geophysical Research Letters*, 38(12). doi: 10.1029/2011GL047563
- von Storch, H., & Zwiers, F. (2002). *Statistical analysis in climate research*. Cambridge University Press.
- Wang, Y., & Huang, Y. (2020). Understanding the atmospheric temperature adjustment to co2 perturbation at the process level. *Journal of Climate*, 33(3), 787 - 803. doi: 10.1175/JCLI-D-19-0032.1
- Xu, J.-S. (1992). On the relationship between the stratospheric quasi-biennial oscillation and the tropospheric southern oscillation. *Journal of Atmospheric Sciences*, 49(9), 725 - 734. doi: 10.1175/1520-0469(1992)049<0725:OTRBTS>2.0.CO;2

Supporting Information for “What contributes to the inter-annual variability in tropical lower stratospheric temperatures?”

Alison Ming¹, Peter Hitchcock²

¹Department of Applied Mathematics and Theoretical Physics, University of Cambridge, Cambridge, UK

²Cornell University, Ithaca, New York, USA

Introduction The supplementary information contains figures that show the same data as the main paper but on different pressure levels or latitudes. It also includes difference plots. Please refer to the main text for a description of the methods.

Contents of this file

1. Figure S1: Time series of ozone interannual variability averaged between 30°N – S
2. Figure S2: Time series of water vapour interannual variability averaged between 30°N – S
3. Figure S3: Difference between ERA5 temperatures and IEFDH calculation
4. Figure S4: IEFDH calculation at 90 hPa
5. Figure S5: Ozone POP time series averaged between 10°N – S
6. Figure S6: IEFDH calculation for QBO ozone at 90 hPa
7. Figure S7: Radiative relaxation rates, α .

8. Figure S8: Enhancement in dynamical heating, β

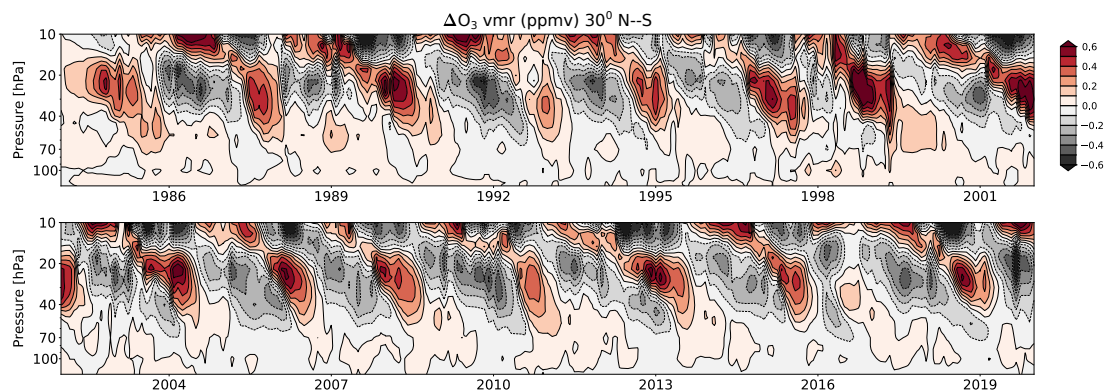


Figure S1. Time series of interannual variations in ozone (in ppmv) from the SWOOSH dataset averaged between 30°N – S.

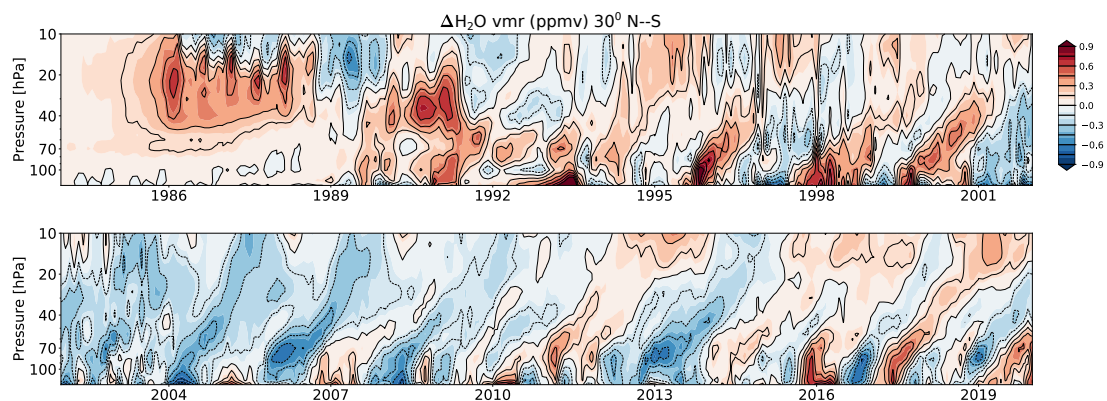


Figure S2. Time series of interannual variations in water vapour (in ppmv) from the SWOOSH dataset averaged between 30°N – S.

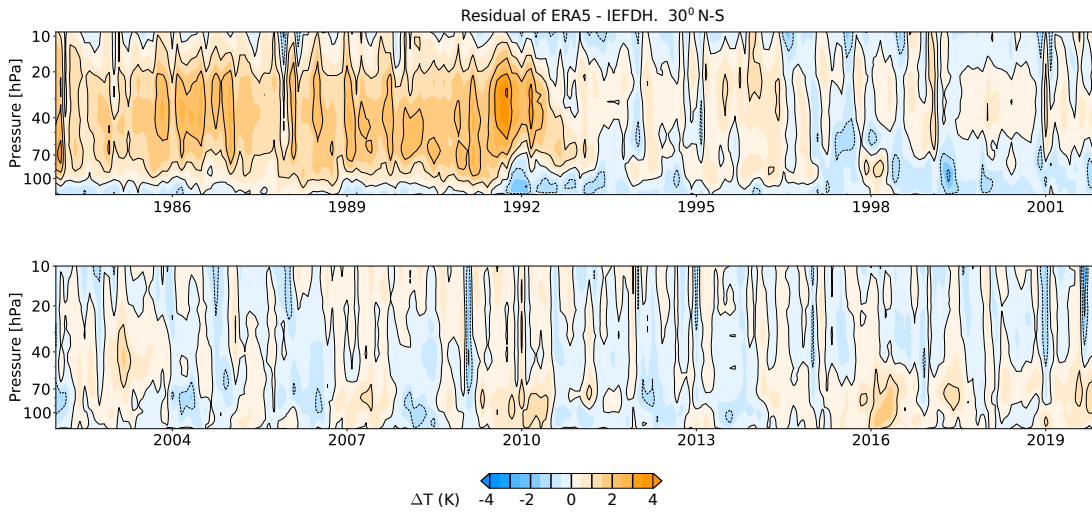


Figure S3. Difference between ERA5 temperatures, Figure 1(a) and IEFDH calculation, Figure 1(b). Values are averaged between 30°N – S.

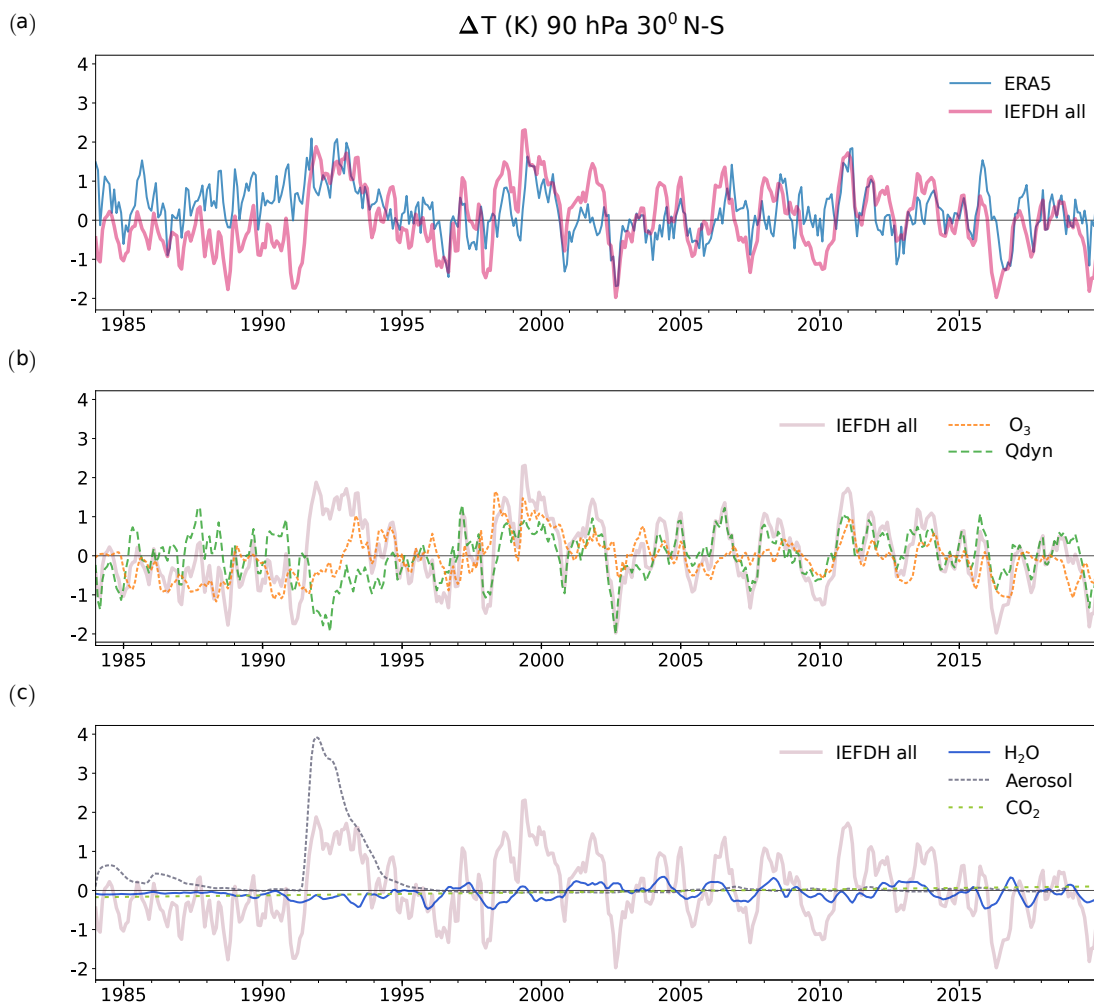


Figure S4. Similar to Figure 2 but at 90hPa. Interannual variability in temperature averaged between 30°N – S, evaluated with respect to the reference period 2002–2010 for (a) ERA5 (cyan line) and the IEFDH all perturbations radiative calculation (thick pink line). The individual contributions to the total are broken down into the those from (b) ozone (orange dotted line) and dynamical heating (green dashed line) and (c) water vapour (blue solid line), aerosol (dotted grey line) and carbon dioxide (green dashed line). In (b) and (c), the IEFDH all perturbations temperature change from (a) is plotted again as the thick pale pink line.

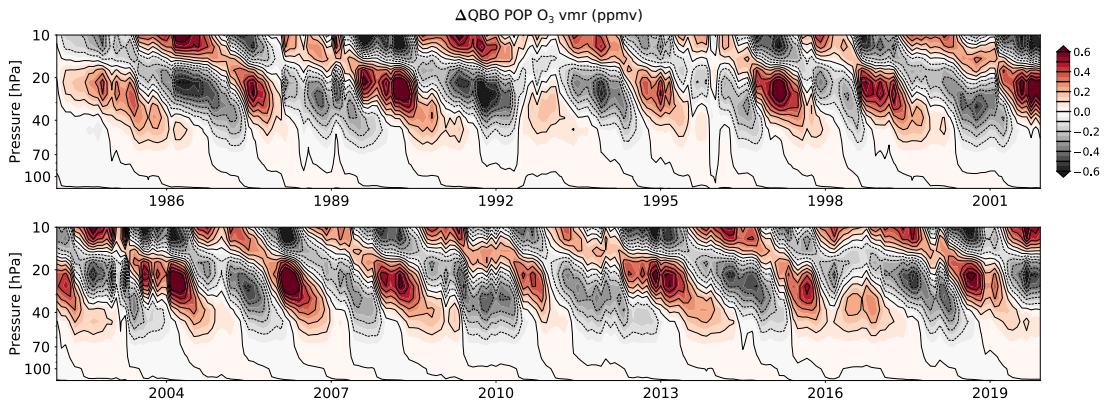


Figure S5. Time series of ozone (in ppmv) associated with the main QBO ozone POP averaged between $10^\circ\text{N} - \text{S}$.

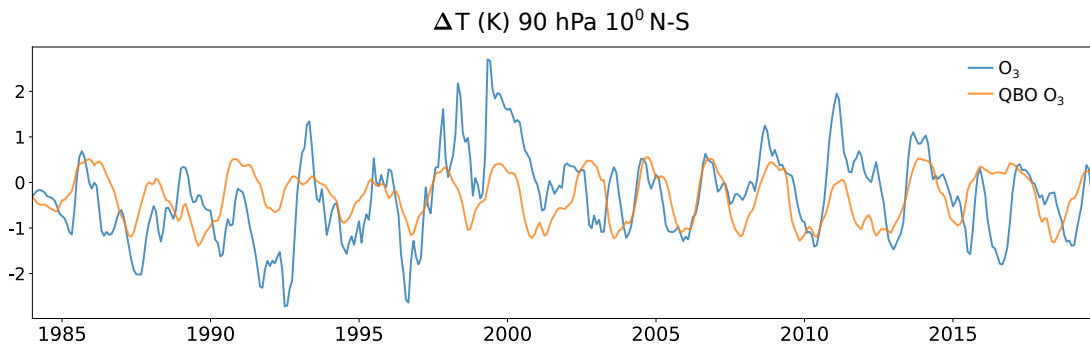


Figure S6. Similar to Figure 3(a) but at 90hPa. IEFDH temperature change (K), averaged between $10^\circ\text{N} - \text{S}$, from interannual variability in ozone and from the leading QBO ozone principle oscillation pattern time series.

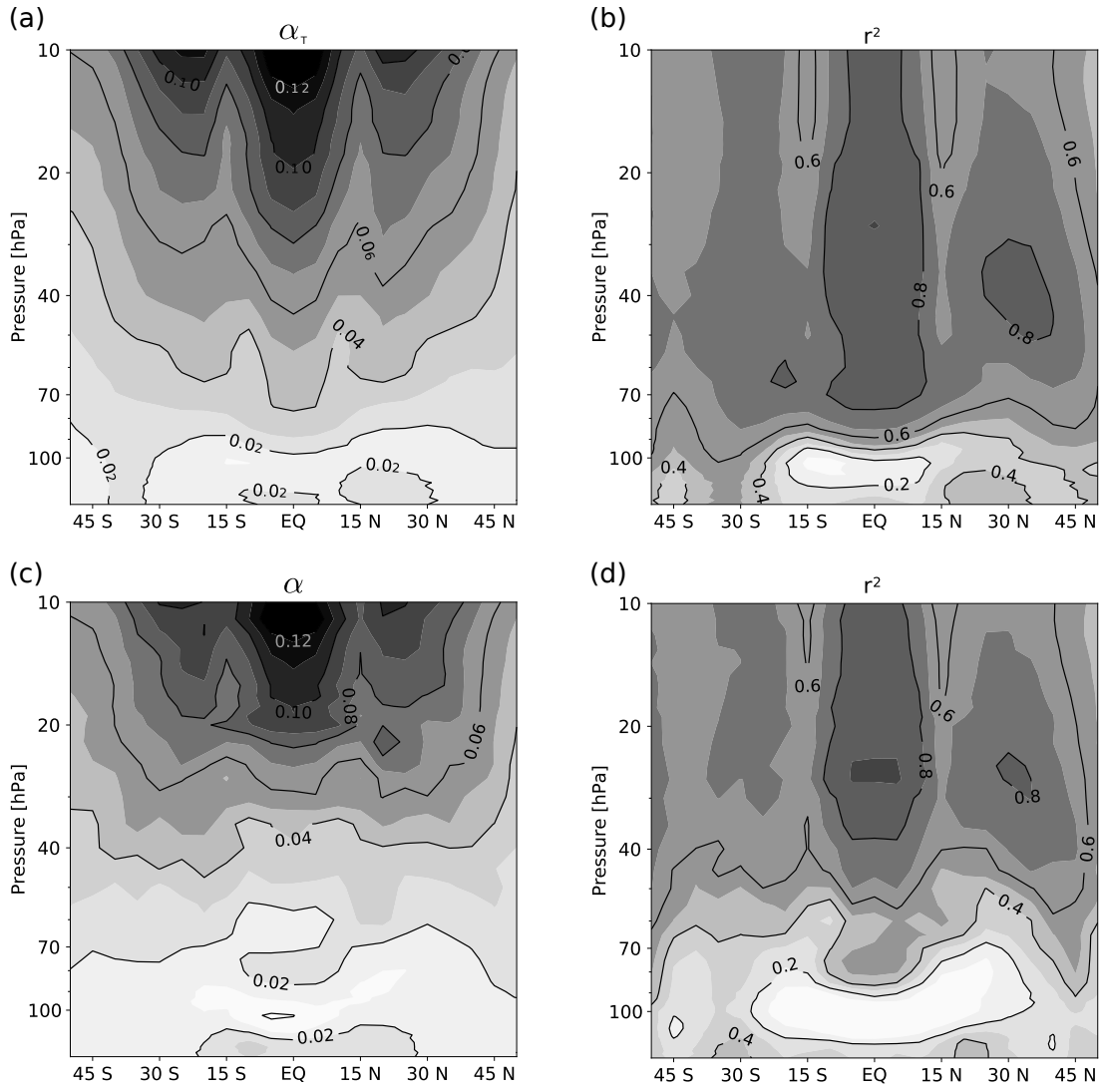


Figure S7. (a) Similar to Figure 6(b) (solid blue line) but showing the variation in latitudes for α_T . (b) Similar to Figure 6(c) (solid blue line), showing the corresponding r^2 . (c) Similar to Figure 6(b) (dashed orange line) but showing the variation in latitudes for α . (d) Similar to Figure 6(c) (dashed orange line), showing the corresponding r^2 .

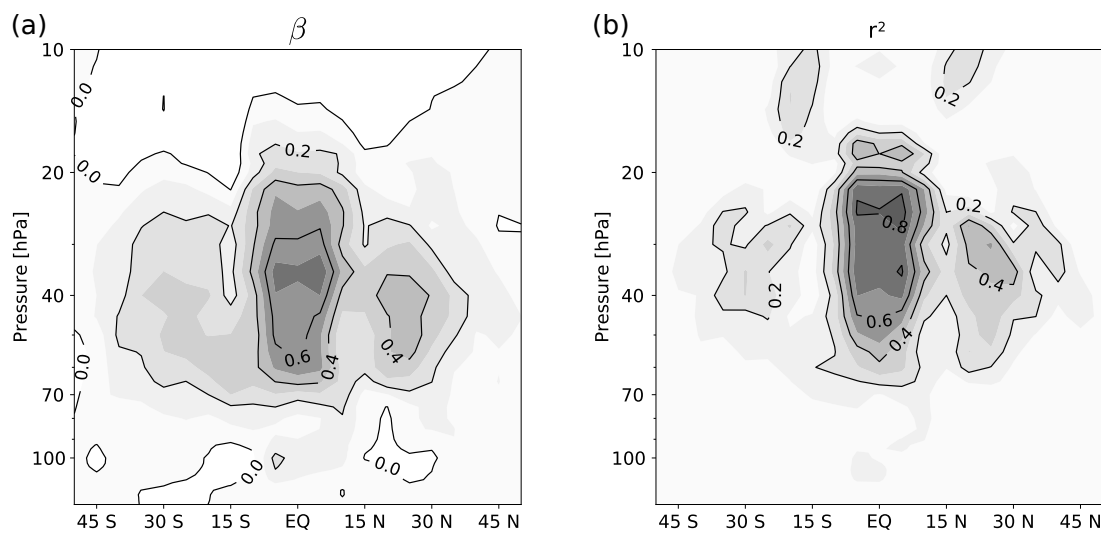


Figure S8. (a) Similar to Figure 7(a) but showing the variation in latitudes for β . (b)

Similar to Figure 7(b), showing the corresponding r^2 .